Nanoscale

PAPER

View Article Online
View Journal | View Issue



Cite this: *Nanoscale*, 2016, **8**, 6820

# Engineering a multi-biofunctional composite using poly(ethylenimine) decorated graphene oxide for bone tissue regeneration†

Sachin Kumar,[a] Shammy Raj,[a] Kishor Sarkar[b] and Kaushik Chatterjee*[a]

Received 6th October 2015,
Accepted 14th February 2016

DOI: 10.1039/c5nr06906h

www.rsc.org/nanoscale

Toward preparing strong multi-biofunctional materials, poly(ethylenimine) (PEI) conjugated graphene oxide (GO_PEI) was synthesized using poly(acrylic acid) (PAA) as a spacer and incorporated in poly-(ε-caprolactone) (PCL) at different fractions. GO_PEI significantly promoted the proliferation and formation of focal adhesions in human mesenchymal stem cells (hMSCs) on PCL. GO_PEI was highly potent in inducing stem cell osteogenesis leading to near doubling of alkaline phosphatase expression and mineralization over neat PCL with 5% filler content and was ≈50% better than GO. Remarkably, 5% GO_PEI was as potent as soluble osteoinductive factors. Increased adsorption of osteogenic factors due to the amine and oxygen containing functional groups on GO_PEI augment stem cell differentiation. GO_PEI was also highly efficient in imparting bactericidal activity with 85% reduction in counts of *E. coli* colonies compared to neat PCL at 5% filler content and was more than twice as efficient as GO. This may be attributed to the synergistic effect of the sharp edges of the particles along with the presence of the different chemical moieties. Thus, GO_PEI based polymer composites can be utilized to prepare bioactive resorbable biomaterials as an alternative to using labile biomolecules for fabricating orthopedic devices for fracture fixation and tissue engineering.

## 1. Introduction

In recent years, graphene and graphene derived particles have received significant interest for their biomedical applications in sensing,[1] imaging,[2] cancer therapy,[3] tissue engineering,[4] and drug and gene delivery[5] owing to their unique properties. Despite the many attractive properties, cytotoxicity of graphene is a critical concern for biomedical applications *in vivo*. The toxicity depends on the concentration, size and functionalization, in addition to other variables such as the fabrication route, the cell type used for measurements *in vitro* and the mode and duration of exposure *in vivo.* However, it appears that a low dose of functionalized graphene, especially when embedded in a polymer, may not be highly toxic[6] and could be investigated for biomedical applications pending a better understanding of long term outcomes *in vivo*.

Graphene can be used to reinforce polymers for biomedical use for load bearing orthopedic applications. We have recently incorporated graphene in a polyethylene composite for improving its mechanical properties for potential use in prosthetic joints.[7] Soft biodegradable polymers are processed to engineer tissue scaffolds and resorbable fracture fixation devices. Graphene can be particularly useful in strengthening such polymers for load bearing orthopedic applications. Graphene offers many advantages over hydroxyapatite and nanosilicate.[8] Fillers such as hydroxyapatite, nanosilicate and bioactive glasses are well established inorganic bioactive particles but their low toughness, low flexural strength and brittleness limit their use in polymeric systems for bone regeneration.[9] Graphene particles have the ability to induce stem cell osteogenesis similar to that of bone morphogenic protein (BMP-2) and other bioactive inorganic materials like hydroxyapatite and nanosilicate.[10,11] Compared to other two dimensional 2D nanoparticles like silicate (clay), layered double hydroxides (LDHs) and transitional metal oxides and dichalcogenides (TMO and TMD), graphene derived particles offer a combination of high surface area and excellent mechanical, electrical, thermal and antibacterial properties[12,13] thereby imparting multifunctionality.

Polyesters such as poly(ε-caprolactone) (PCL) are widely utilized in biodegradable applications including sutures and patches approved for clinical use. Even at low filler content graphene and its derivatives can significantly improve the

[a]*Department of Materials Engineering, Bangalore 560012, India. E-mail: kchatterjee@materials.iisc.ernet.in; Tel: +91-80-22933408*
[b]*Department of Chemical Engineering, Indian Institute of Science, Bangalore 560012, India*
†Electronic supplementary information (ESI) available. See DOI: 10.1039/c5nr06906h

modulus and strength of PCL.[12] Bioactive substrates that provide suitable mechanical, chemical and biological cues can promote cell proliferation and differentiation.[14,15] Aside from strengthening, graphene can be functionalized to improve the bioactivity of the composite or applied as a surface coating on a biomaterial substrate.[16] Shin *et al.* recently showed that the graphene–hydroxyapatite hybrid was more effective in inducing osteogenesis than individual nanoparticles.[17] We reported that graphene–strontium hybrid nanoparticles in PCL scaffolds promoted osteogenesis for bone tissue engineering.[18]

The surface chemistry of a biomaterial is a potent tool to control the biological response.[15] GO with a large surface area rich in oxygen containing functional groups such as carboxyl, hydroxyl, carbonyl and epoxide moieties provide many opportunities for chemical modification. In our previous study, we functionalized GO with methylene dianiline (MDA) yielding amine-functionalized GO (AGO). AGO in the PCL composite provided an optimal combination of increased modulus, enhanced stem cell growth and differentiation, and inhibition of biofilm formation for orthopedic applications, which was attributed to the mixture of amine and oxygen containing moieties on AGO.[19] Whereas graphene–metallic hybrid nanoparticles promoted osteogenesis due to the release of bioactive ions,[17,18] AGO particles enhanced stem cell osteogenesis and inhibited bacterial growth.[19] For orthopedic biomaterials that require good mechanical properties, bioactivity and antibacterial activity, multi-amine functionalized graphene can be highly effective.

Branched poly(ethylenimine) (PEI) with a high density of amine groups has extensive use in biomedical applications, in particular for gene transfection.[20] PEI is more efficient than chitosan and poly-D-lysine in promoting cell attachment.[21] PCL/PEI blend nanofibers facilitated the spreading of fibroblasts compared to neat PCL but induced toxicity at higher concentration due to the cationic nature of high molecular weight PEI.[22] We propose that GO decorated with PEI (GO_PEI) can be used to increase the amine groups on GO in contrast to MDA-modified AGO where MDA offers only a single free amine to yield multi-biofunctional polymer composites. GO grafted with PEI showed good gene transfection efficiency.[23] Weng *et al.* have shown that GO functionalized with PEI have an excellent protein binding ability even in very dilute solutions and also in complex biological fluids.[24] Whereas it has been reported that PEI and GO functionalized with PEI help in better cell attachment and binding of protein and DNA, the potential advantage of GO functionalized with PEI in preparing multifunctional biomaterials for bone tissue regeneration has not been studied.

The objective of this work was to synthesize and characterize GO_PEI. To improve the grafting efficiency, polyacrylic acid (PAA) was used as the spacer molecule to enhance the availability of carboxyl groups on GO. Low molecular weight branched PEI was used to minimize cytotoxicity. The physicochemical properties of the composites of GO_PEI in PCL at different filler content were compared to GO composites and neat PCL. The resultant effect on stem cell proliferation, induction of stem cell osteogenesis and bacterial cell viability was systematically studied to prepare multi-biofunctional composites.

## 2. Experimental

### 2.1 Synthesis of GO and GO_PEI particles

GO was synthesized by chemical oxidation of graphite (Sigma) according to the Hummers method[25] with some modifications, as reported previously.[19] PEI conjugated GO (GO_PEI) was synthesized *via* a two-step process including the grafting of PAA with GO through free radical polymerization followed by conjugation of low molecular weight PEI (2 kDa) with the carboxylic acid groups of PAA as shown schematically in Fig. 1(a).

**2.1.1 Synthesis of graphene oxide-grafted polyacrylic acid (GO-*g*-PAA).** 50 mg of GO was added into 50 ml distilled water and dispersed by sonication. The dispersed GO solution was transferred to a 100 ml three-necked round bottom flask and placed in an oil bath. The solution was degassed by bubbling $N_2$ gas for 30 min followed by the addition of 10 ml aqueous ammonium persulfate (APS) solution (1 wt% of GO) and stirred continuously for 10 min at 60 °C under a $N_2$ atmosphere. 1.0 g acrylic acid passed through a basic alumina column was added dropwise to the above solution under constant stirring under a $N_2$ atmosphere. The reaction was continued further for 3 h at 60 °C under a $N_2$ atmosphere. The reaction was stopped by bringing the reaction system in contact with air and then cooled down to room temperature. The reaction mixture was centrifuged and washed several times with water to remove the water soluble homopolymer of PAA. Finally, the purified product was lyophilized for 3 days to obtain GO-*g*-PAA.

**2.1.2 Synthesis of PEI conjugated GO-*g*-PAA (GO_PEI).** 50 mg GO-*g*-PAA was dispersed in 25 ml 5 mM MES buffer (2-(*N*-morpholino) ethanesulfonic acid). Excess equimolar of EDC [1-ethyl-3-(3-dimethylaminopropyl) carbodiimide] and NHS (*N*-hydroxy succinimide) (Sigma) were added to the above dispersion and stirred for 1 h at room temperature to activate the carboxylic acid groups of GO-*g*-PAA. An aqueous solution of low molecular weight (2 kDa) branched PEI (Sigma) (2.0 g) was added to the above mixture and stirred continuously for 24 h at 23 °C. The solution was centrifuged and washed several times with water to remove unreacted reactants. Finally the solution was lyophilized for 3 days to obtain the PEI conjugated GO.

### 2.2. Characterization

Synthesized GO, GO-*g*-PAA and GO_PEI nanoparticles were chemically characterized using Fourier transform infrared spectroscopy (FTIR, PerkinElmer Frontier IR/NIR systems, USA) from 4000 to 650 $cm^{-1}$. The chemical composition of GO and modified GO was evaluated using an X-ray photoelectron spectrometer (XPS, PHI 1257, PerkinElmer, USA). The surface modification of GO and GO_PEI was characterized using an atomic force microscope (AFM, NanoWizardR 3, JPK Instru-

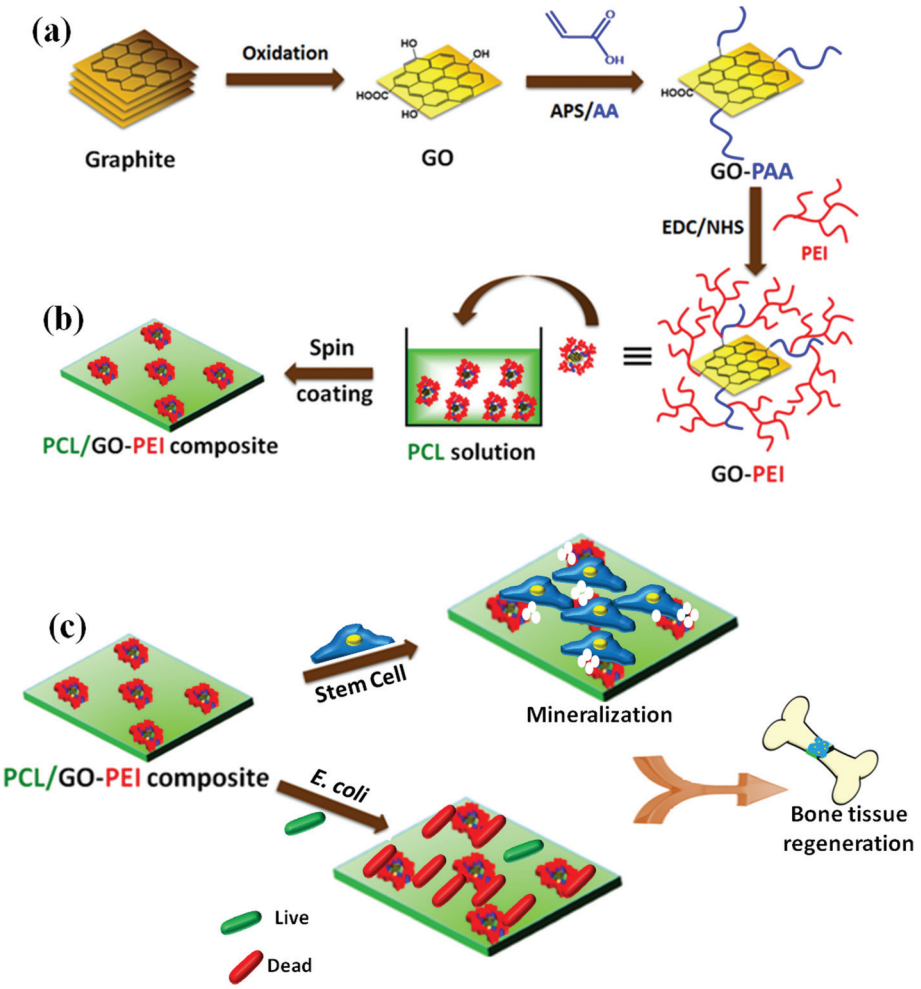


**Fig. 1** Schematic representation of (a) the synthesis of GO, GO-*g*-PAA and GO_PEI nanoparticles, (b) preparation of PCL/graphene composite films by spin coating and (c) biological studies showing stem cell and bacterial response to PCL/graphene composites for potential orthopedic use.

ments) in tapping mode. Ultraviolet visible (UV-vis) spectroscopy measurements were performed on GO, GO-*g*-PAA and GO_PEI particles dispersed in distilled water using a UV-1700 spectrophotometer (Shimadzu). The X-ray diffraction (XPERT-Pro, PANalytical, UK) patterns were obtained using a Cu Kα radiation source ($\lambda$ = 1.5406 Å, 40 kV, and 20 mA). Thermal gravimetric analysis (TGA) was performed using a NETZSCH STA 409 at a constant heating rate of 20° C $min^{-1}$ under an inert argon atmosphere. GO_PEI was also analyzed by Raman spectroscopy (WITEC Raman spectrometer, Germany) using an optical excitation source of a 514 nm wavelength laser.

### 2.3 Preparation and characterization of PCL/GO and PCL/GO_PEI composites

Thin films of PCL/GO and PCL/GO_PEI composites and neat PCL were prepared by the spin coating technique (Fig. 1(b)). The synthesized GO and GO_PEI nanoparticles were dispersed in THF using a bath sonicator (S.V. Scientific) for 1 h. PCL was added at 0.1 g $mL^{-1}$ and stirred for 24 h. The weight fraction of graphene nanoparticles was varied from 1 wt% to 5 wt% of the polymer as listed in Table 1. The solution was spin coated on an aluminum substrate at 2500 rpm for 30 s to obtain a uniform film of the polymer composite on the substrate. The spin coated samples were dried in a desiccator for 24 h under vacuum. Dried spin coated samples were cut into circular discs of 10 mm diameter. The morphology, thickness and roughness of the samples were characterized using a scanning electron microscope (SEM, ESEM Quanta 200, FEI), an AFM

**Table 1** Nomenclature and composition of the different samples

| | Composition | |
|---|---|---|
| Sample code | mg of GO per g of PCL | mg of GO_PEI per g of PCL |
| PCL | 0 | 0 |
| PCL/GO_1 | 10 | 0 |
| PCL/GO_3 | 30 | 0 |
| PCL/GO_5 | 50 | 0 |
| PCL/GO_PEI_1 | 0 | 10 |
| PCL/GO_PEI_3 | 0 | 30 |
| PCL/GO_PEI_5 | 0 | 50 |

and an optical profilometer (Talysurf CCI, Hobson). The surface hydrophobicity of the composites films was determined using a digital contact angle goniometer (OCA 15EC, Dataphysics, USA). The minimum of three independent measurements was taken on the films and the data are reported as mean ± standard deviation (S.D.). To evaluate the mechanical properties of PCL and its composites, each of the abovementioned solutions of PCL, PCL/GO and PCL/GO_PEI was precipitated using methanol. The precipitate was vacuum dried at 25 °C for 48 h. Rectangular samples (length × width × thickness = 25 mm × 10 mm × 0.5 mm) were prepared by compression molding. Dynamic mechanical analysis (DMA Q800, TA Instruments) was performed to evaluate storage modulus of samples in accordance with our previous report.[19]

### 2.4 Biological studies

Fig. 1c schematically presents the study of responses of stem cells and bacteria to the spin coated PCL/graphene composite films *in vitro* to assess their potential use in orthopedics.

**2.4.1 Cell studies.** Primary bone-marrow derived human mesenchymal stem cells (hMSCs) from a male patient aged 25 years (Stempeutics, India) were cultured in standard culture flasks in complete culture medium prepared from Knockout Dulbecco's modified Eagle medium (DMEM, Invitrogen) supplemented with 1% glutamax, and a 1% penicillin–streptomycin antibiotic mixture (Sigma) and 15 vol% MSC qualified fetal bovine serum (FBS, Himedia). The culture flask was incubated under a 5% $CO_2$ atmosphere at 37 °C. The medium was changed twice per week until 70–80% confluency was reached. Cells were lifted using 0.25% trypsin (Gibco) and seeded on the composite films. Prior to cell seeding, the spin coated films were cut into circular discs of 10 mm diameter and placed in 48-well plates. All disc samples were sterilized in combination with 70% ethanol under UV for 30 min. $3 \times 10^3$ cells were added into each well with 0.5 mL of complete culture medium.

**2.4.2 Stem cell proliferation and morphology.** The attachment, morphology and proliferation of hMSCs on the composite films were assessed 1, 3 and 7 days after cell seeding using a combination of the DNA quantification assay and fluorescence imaging. The cell numbers on the films were determined by measuring the DNA content on each sample using the Picogreen assay (Invitrogen). In order to quantify the DNA content, hMSCs on the disc samples were lysed using 200 μl lysis solution (0.2 mg $mL^{-1}$ proteinase K (Sigma) and 0.02% sodium dodecyl sulfate (Sigma)). Samples were incubated at 37 °C for 24 h. 100 μl of the lysate solution was mixed with 100 μl of the Picogreen working solution. Fluorescence intensity reading of the solution was measured using a microplate reader (Biotek, USA) at 485 nm excitation and 528 nm emission. A total of six samples ($n = 6$) of each composite were used to quantify DNA content. hMSCs on the films were fixed with 3.7% formaldehyde for 30 min and permeabilized using 0.2% Triton X-100 (Sigma). The nuclei were stained with DAPI (14.3 mM, Invitrogen) for 5 min to microscopically study cell attachment and proliferation at day 1, 3 and 7 using an epi-fluorescence microscope (Olympus IX-71).

Viability of hMSCs on PCL, PCL/GO_5 and PCL/GO_PEI_5 surfaces was assessed using the live/dead staining assay. At day 3 and 7 culture medium was changed. Cells were stained with the live/dead reagents (calcein and ethidium homodimer-1, Invitrogen) according to the instructions of the supplier. Live and dead hMSCs on the substrates were imaged using an epi-fluorescence microscope in the green and red channels, respectively.

To characterize the cell morphology at day 1 and 3, hMSCs were fixed on the composite films with 3.7% formaldehyde for 30 min and permeabilized using 0.2% Triton X-100 (Sigma). 6.6 μM Alexa Fluor 546 and 1 μM Sytox green (both from Invitrogen) were used to stain actin filaments and nuclei for 30 min and 15 min, respectively. Stained hMSC were imaged in the red and green channels, respectively, of the inverted fluorescence microscope. ImageJ software was used to quantify the stem cell area and the aspect ratio. A cell outline was created to measure the cell area and the aspect ratio was calculated by fitting an ellipse.

To examine focal adhesions, cells at day 3 were fixed with 3.7% formaldehyde for 30 min and permeabilized with 0.2% Triton X-100. 0.2% fish skin gelatin in PBS and 0.02% Tween were used for blocking for 45 min at room temperature. The cells were incubated with the primary antibody (Paxillin, Abcam 2264) diluted (1 : 200) with blocking buffer overnight at 4 °C. An anti-rabbit secondary antibody conjugated with Cy3 (red) was used. Cells were incubated with the secondary antibody for 45 min at room temperature. The nuclei and actin filaments were stained with DAPI (blue) and Alexa Fluor 488 (green) for 5 and 30 min. Cells were imaged using a confocal microscope (Zeiss, LSM 710).

**2.4.3 Osteogenic differentiation.** Osteogenic differentiation of hMSCs was studied by measuring the alkaline phosphatase (ALP) activity in growth medium and in a medium supplemented with osteoinductive factors (10 nM dexamethasone, 20 mM β-glycerophosphate and 50 μM ascorbic acid, all procured from Sigma). ALP expression was measured using *p*-nitrophenyl phosphate (pNPP, Sigma) at 14 and 21 days in accordance with our previous study.[26]

hMSCs were cultured on the spin coated samples in growth medium and in osteoinductive medium to assess *in vitro* mineralization at 14 and 21 days. Calcium mineral deposited by hMSC on the films was quantified using the Alizarin red S dye (ARS, Sigma) as reported previously.[19] Briefly, the medium was aspirated and hMSCs were fixed using 3.7% formaldehyde solution for 30 min and stained with 2% ARS. For mineral quantification, ARS stained mineral nodules were dissolved in 0.2 mL of 5% SDS in 0.5 N HCl for 30 min. The absorbance of the solubilized dye was read at 405 nm using a microplate reader (BioTek). Furthermore, the mineralized films were imaged using the SEM and the chemical nature of the mineral deposited on the composite surface was analyzed by energy dispersive X-ray (EDX) spectroscopy.

DNA quantification was performed at 14 and 21 days using the Picogreen assay as described above. ALP activity and mineral content were normalized to DNA content, which is taken as a measure of cell number.

### 2.5 Adsorption of osteogenic factors

Adsorption of soluble osteogenic factors on graphene composites was evaluated in accordance with the literature with slight modifications.[27] Individual solutions of β-glycerol phosphate, dexamethasone and ascorbic acid were prepared in distilled water having a concentration of 10 mM. PCL, PCL/GO_5 and PCL/GO_PEI_5 composite films were incubated with each factor for 3 days at 37 °C. Thereafter, films with adsorbed factors were placed individually in tubes having fresh distilled water and sonicated for 15 min to remove surface adsorbed molecules. The absorbance of the solution was measured using a well plate reader in the wavelength range of 200–250 nm. Each adsorption study was performed with three independent samples from each group.

### 2.6 Antibacterial study

The direct contact method was employed to evaluate antibacterial properties of PCL, PCL/GO and PCL/GO_PEI composite discs.[28,29] Overnight culture of *Escherichia coli* (ATCC 25922) grown in sterile Luria Broth (LB) at 200 rpm and 37 °C was diluted to adjust the bacterial suspension turbidity to 0.5 optical density (OD) at 600 nm. Sterilized samples were placed in 48 well polystyrene plates. 200 μL of bacterial suspension (of 0.5 OD) was placed on the surface of each sample. Plates were incubated at 37 °C for 2 h. Thereafter, the cell suspension was removed and the films were washed several times with sterile 0.9% saline solution in order to remove the non-adherent bacteria. Samples were transferred to a centrifuge tube with 5 mL saline solution. To remove the adhered bacteria from the sample surface, tubes were bath sonicated for 5 min. The bacterial suspension was diluted and mixed using a vortex mixer for 10 s. Diluted *E. coli* suspensions from each sample were spread and plated on LB agar plates and incubated at 37 °C for 24 h. *E. coli* colonies on agar plates were photographed and counted. All the results represent the average colony count from three independent plates for each sample. For the imaging of *E. coli* adhered to the samples, the bacteria on the samples were washed and fixed using 2.5% aqueous glutaraldehyde solution for 30 min. Samples were dried in a dessicator under vacuum for 24 h and coated with gold prior to SEM imaging.

To evaluate the viability of *E. coli* on the samples the live/dead assay was performed as follows. 200 μl of *E. coli* suspension was placed on each test sample and allowed to attach for 2 h as described above. Samples were washed thrice and 100 μl of the live/dead dye (BacLight, Invitrogen) was used to stain bacterial cells and incubated in the dark for 15 min before fluorescence imaging. Dead bacteria on the sample appear red whereas live bacterial cells appear green. Stained cells were quantified from at least five different fields of at least three independent replicates.

### 2.7 Statistical analysis

Statistically significant differences between the samples were analyzed using 1-way ANOVA (analysis of variance) with a Tukey's test for multiple comparisons. Differences were considered statistically significant for $p < 0.05$ and indicated by symbols in the respective figures.

## 3. Results and discussion

### 3.1 Synthesis and characterization of GO and GO_PEI particles

There are many reports on the conjugation of PEI on to the GO surface using different techniques. Direct covalent conjugation of PEI on to the surface of GO is one of the most common strategies. The carbodiimide crosslinking reaction has been widely used to covalently conjugate PEI to GO through the formation of an amide linkage between the –COOH functional groups of GO and $–NH_2$ groups of PEI.[23] However, the –COOH functional groups are typically present along the perimeter of the GO sheets, which limits the extent of PEI functionalization of GO. Thus, we aimed to increase the presence of –COOH functional groups on GO to maximize PEI functionalization. PAA with numerous –COOH groups has been successfully grafted on to the GO surface.[30] GO grafted PAA nanoparticles have been shown to be an effective protein and drug carrier with minimal cytotoxicity.[30,31] In this work, PAA was chemically grafted on to GO to enhance the availability of –COOH groups for augmenting the extent of PEI functionalization, thereby yielding GO_PEI particles richer in amine and oxygen functional groups than GO.

GO-*g*-PAA particles were synthesized by grafting acrylic acid chains onto the GO surface by free radical polymerization using APS as the radical generator.[31,32] The free radical site was generated by removing the hydrogen from the –OH group on the GO surface which assisted in polymerization of acrylic acid on the GO surface. PEI was conjugated on the synthesized GO-*g*-PAA particles by covalent linking between –COOH groups of GO-*g*-PAA particles and $–NH_2$ groups of PEI using EDC/NHS chemistry. FTIR spectra of GO, GO-*g*-PAA, PEI and GO_PEI are shown in Fig. 2(a). Broad and narrow intense peaks at ≈3300 $cm^{-1}$, 1736 $cm^{-1}$ and 1625 $cm^{-1}$ represent characteristic stretching of –OH, C═O of –COOH groups and C═C vibration of aromatic chains on the GO surface. GO also showed peaks at 1369 $cm^{-1}$, 1220 $cm^{-1}$ and 1050 $cm^{-1}$ representing carboxyl/carbonyl, epoxy, and alkoxy groups, respectively.[33] In contrast, GO-*g*-PAA exhibited peaks for all the functional groups for GO along with new peaks at 2925 $cm^{-1}$, 2853 $cm^{-1}$ and 803 $cm^{-1}$, which may be attributed to the stretching and bending of $–CH_2$ and –OH groups from PAA.[30] Thus, the new peaks on GO-*g*-PAA indicate successful polymerization of acrylic acid on the GO surface.

PEI showed doublet peaks at 3365 $cm^{-1}$ and 3285 $cm^{-1}$ corresponding to the stretching of the $–NH_2$ group and intense peaks at 2940 $cm^{-1}$ and 2810 $cm^{-1}$, which may be assigned to the stretching of $–CH_2$. PEI also showed characteristic peaks at 1590 $cm^{-1}$, 1455 $cm^{-1}$ and 1290 $cm^{-1}$ due to –NH bending, –CH bending and –CN stretching.[34] GO_PEI flakes clearly showed characteristic groups of both GO-*g*-PAA and PEI. It showed two peaks at 2938 $cm^{-1}$ and 2830 $cm^{-1}$ featuring $–CH_2$

 

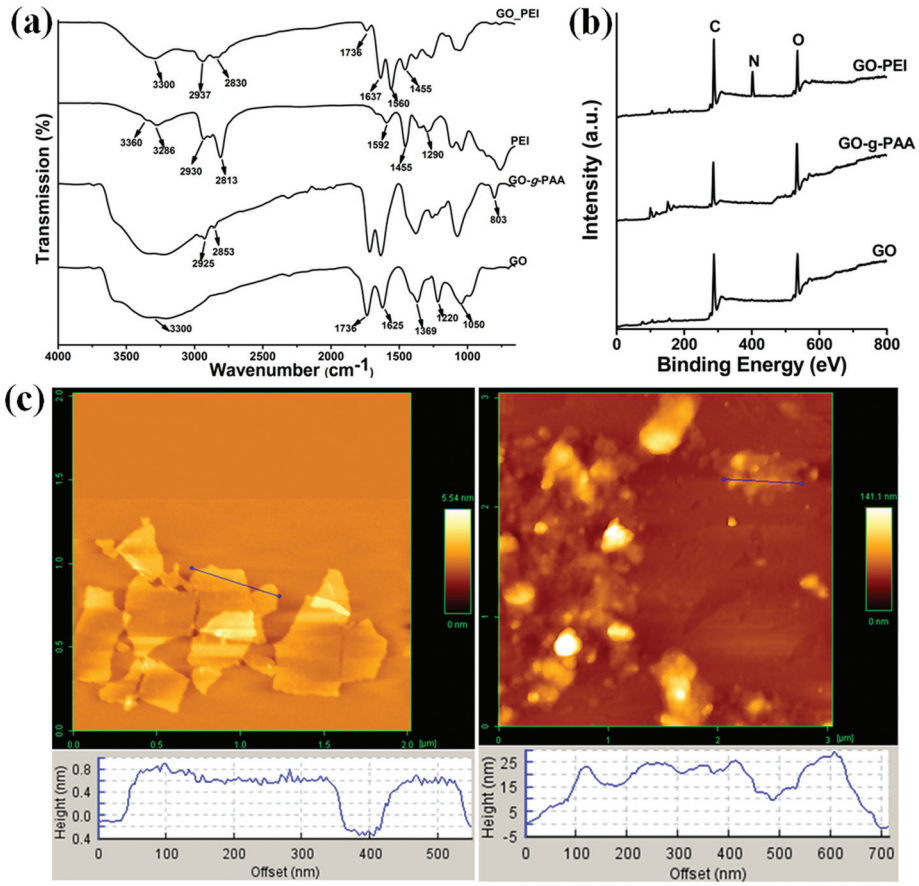


Fig. 2 Characterization of the synthesized nanoparticles: (a) FTIR spectra of GO, GO-*g*-PAA, PEI and GO_PEI, (b) XPS spectra for GO, GO-*g*-PAA and GO_PEI, (c) AFM images with flake thickness profiles of GO and GO_PEI.

stretching from PEI chains. A sharp decrease in the peak intensity at 1740 $cm^{-1}$ and the appearance of a new peak at 1637 $cm^{-1}$ indicate the formation of an amide linkage between GO-*g*-PAA and PEI.[35] Furthermore, GO_PEI showed peaks at 1560 $cm^{-1}$ and 1455 $cm^{-1}$ due to bending of –NH and –CH groups of the PEI molecule. Note that we compared the direct grafting of PEI on pristine GO with GO-*g*-PAA (Fig. S1†). GO_PEI (PEI grafted on GO-*g*-PAA) showed more intense peaks for –NH, –CH and –CN stretching at 1560 $cm^{-1}$, 1455 $cm^{-1}$ and 1283 $cm^{-1}$ compared to GO-*g*-PEI (PEI grafted directly on pristine GO). The presence of these intense peaks of PEI on GO_PEI flakes suggested that the use of PAA as a spacer resulted in more efficient grafting of PEI, thereby demonstrating the utility of the strategy presented here. Thus, the presence of an amide bond and multiple intense peaks of PEI on GO-*g*-PAA confirm the conjugation of PEI on the GO-*g*-PAA surface.

Fig. 2(b) shows a wide energy spectra scan for GO, GO-*g*-PAA and GO_PEI. Pristine GO, GO-*g*-PAA and GO_PEI spectra showed characteristic C 1s and O 1s peaks at 286 and 534 eV, respectively. In the case of GO and GO-*g*-PAA, only carbon and oxygen peaks were observed. However, the intensity of the oxygen peak is more than carbon for GO-*g*-PAA in comparison with GO. This may be attributed to the polymerization of AA on the GO surface. GO_PEI showed the presence of an additional N 1s peak at 400 eV. The presence of the nitrogen peak on GO_PEI further confirms the conjugation of nitrogen enriched PEI molecules to GO-*g*-PAA. During PEI conjugation by EDC and NHS, a decrease in oxygen content is commonly reported to be an indication of successful grafting of PEI.[36,37] The atomic composition of GO, GO-*g*-PAA and GO_PEI are listed in Table S1.† AFM micrographs of GO and GO_PEI flakes are shown in Fig. 2(c). The sheet thickness increased from ≈0.8 nm for GO to ≈20–30 nm for GO_PEI. The increase in thickness can be attributed to grafting of PAA–PEI conjugated on both sides of the GO sheets.

The UV-visible spectra of GO, GO-*g*-PAA and GO_PEI particles dispersed in water are shown in Fig. S2(a).† GO showed a characteristic absorption peak at ≈230 nm, which may be attributed to the π–π* transitions for aromatic C–C bonds and a shoulder at 300 nm for the n–π* transitions of carbonyl groups.[38] GO-*g*-PAA showed a decrease in intensity with the increase in wavelength without showing any intense absorption peaks. GO-*g*-PAA showed two small shoulders at ≈250 and 310 nm. On the other hand, GO_PEI dispersed nanoparticles showed low intensity shoulders (indicated by the blue arrow) at ≈270 nm. Reports have shown that grafting of PEI on the

GO surface not only diminishes but also shifts the 230 nm absorbance peak to 270 nm.[39,40] The shift in the absorbance peak for GO_PEI has been attributed to the restoration of π electron conjugation within graphene sheets,[41] suggesting partial reduction and coverage of GO with PEI.[40] The inset in Fig. S2(a)† shows the color change of GO from dark brown to yellow brownish and to grayish during the synthesis of GO-*g*-PAA and GO_PEI from GO, indicating successful grafting of PAA and PEI on the GO surface.

Fig. S2(b)† shows the XRD diffraction pattern of GO and GO_PEI. GO showed a characteristic diffraction peak at ≈10.85° corresponding to an interlayer distance of 8.2 Å. GO-*g*-PAA showed a shift in the diffraction peak to 9.4° whereas GO_PEI showed a peak at 8.3° representing *d* spacing of 10.6 Å. The increase in the interlayer distance for GO-*g*-PAA and PEI_GO may be attributed to the insertion of the grafted PAA and PEI molecules in the interlayer between GO sheets.[36]

The thermal stability of PAA and PEI grafted GO was evaluated by TGA as shown in Fig. S2(c).† The initial weight loss of GO can be assigned to the removal of surface adsorbed water from the hydrophilic GO surface. A sharp weight loss at ≈200 °C was due to the pyrolysis of liable oxygen containing functional groups from the GO surface.[42] The weight loss up to 200 °C was ≈40%. Above 200 °C, GO decomposed slowly with an additional weight loss of ≈19% between 200 and 500 °C. GO-*g*-PAA showed two step thermal decomposition, at first a continuous weight loss (48%) up to 300 °C that is ascribed to the loss of adsorbed water and thermal decarboxylation of GO-*g*-PAA.[43] The second rapid weight loss of GO-*g*-PAA from 300 to 400 °C may be assigned to the thermal degradation of polymeric chains of PAA grafted on the GO surface.[30] The difference in weight loss at 500 °C of GO and GO-*g*-PAA is ≈20%. GO_PEI showed the initial thermal decomposition pattern matching with GO and GO-*g*-PAA. However, it showed rapid and continuous weight loss after 250 °C due to the pyrolysis of PAA and PEI polymer chains. GO_PEI showed the highest weight loss (97%) at 500 °C in contrast to GO and GO-*g*-PAA suggesting that conjugation of PEI resulted in decreased thermal stability. GO-*g*-PAA and GO_PEI showed more weight loss than GO suggesting the successful grafting of PAA and PEI on GO. The weight fraction of PAA on GO was calculated to be ≈20% whereas PEI conjugation on the GO-*g*-PAA surface was ≈22%.

Raman spectra of GO, GO-*g*-PAA and GO_PEI show two peaks at 1350 and 1600 $cm^{-1}$, which are the characteristic D and G bands, respectively (Fig. S2(d)†). Chemical modifications of graphene derived nanoparticles are often characterized by the changes in the ratio of the area of the D and G bands ($I_D/I_G$).[40,44] The $I_D/I_G$ ratio of GO, GO-*g*-PAA and GO_PEI is 1.21, 1.40 and 1.43, respectively. The increase in the $I_D/I_G$ ratio for both GO-*g*-PAA and GO_PEI suggests that new carbon atoms are grafted on the GO surface.[40] Yang *et al.* reported an increase in the $I_D/I_G$ ratio upon grafting of PEI on the GO surface due to the nucleophilic reaction between carboxyl and amine groups leading to the elimination of oxygen groups and formation of covalent bonds.[45]

### 3.2 Characterization of PCL/GO and PCL/GO_PEI composites

The SEM surface morphologies of spin coated samples of PCL, PCL/GO_5 and PCL/GO_PEI_5 are shown in Fig. 3(a). SEM micrographs of PCL and its different graphene composites showed rounded spherulites without any pores on the surface. Large spherulites were seen in the PCL sample compared to smaller spherulites for PCL/GO and PCL/GO_PEI. Furthermore, GO and GO_PEI nanoparticles were found exposed on the respective composite surface as indicated by the arrow in the SEM micrographs (Fig. 3(a)). It has been shown that during spin coating of a polymer–graphene solution, most of the graphene nanoparticles appear on the surface of the composite as higher contrast particles against the insulating polymer matrix.[46] Similarly, in this study brighter GO and GO_PEI nanoparticles were found exposed on the PCL surface.

AFM images of neat PCL and its composites showed a surface morphology similar to that observed in SEM (Fig. 3(b)). Graphene particles were uniformly dispersed on the surface of the composites (PCL/GO_5 and PCL/GO_PEI_5) films as pointed by arrows in Fig. 3(b). Also, composite films showed a larger number of smaller spherulites than the neat PCL film. More spherulites in composite films suggest an increase in nucleation density in composites, which may be attributed to the heteronucleation induced by the GO filler. It has been shown that reinforcement of GO in the polymer matrix promotes heterogeneous nucleation, resulting in the formation of a large number of smaller spherulites.[47]

Surface wettability of biomaterials not only influences the biological outcome but also affects the kinetics of hydrolytic degradation. Fig. 3(c) shows the surface water contact angle for spin coated neat PCL, PCL/GO and PCL/GO_PEI films. The surface wettability of the composite films scales with the GO and GO_PEI content. The water contact angle of the neat PCL film decreased from 79.6 ± 2.3° to 69.3 ± 1.9° for 5 wt% GO content and to 63.6 ± 2.4° with the addition of 5 wt% GO_PEI. Grafting of PAA and PEI molecules increased the content of hydrophilic polar functional groups like carboxylic, carboxylate and amine groups over that of GO, as indicated by FTIR analysis in Fig. 2(a). The presence of more polar oxygenated functional groups on GO sheets results in increased surface energy of GO.[48] Thus, the presence of the GO and GO_PEI particles in the PCL matrix, as seen in the SEM micrographs (Fig. 3(a)), resulted in the increased surface wettability of PCL.

The thickness of the films determined by profilometry was found to be ≈10 μm for all the samples. However, the average surface roughness ($R_a$) of PCL increased with reinforcement of GO and GO_PEI particles (Table S2†). Surface roughness profiles obtained from profilometry for neat PCL, PCL/GO_5 and PCL/GO_PEI_5 composites are compiled in Fig. 3(d). The presence of GO and GO_PEI nanoparticles on the PCL surface can affect the surface roughness at the nanoscale, which may influence stem cell behavior. Cells are sensitive to changes in surface topography of biomaterials.[49] The storage modulus of PCL and its different composites are listed in Table S2.† The

 

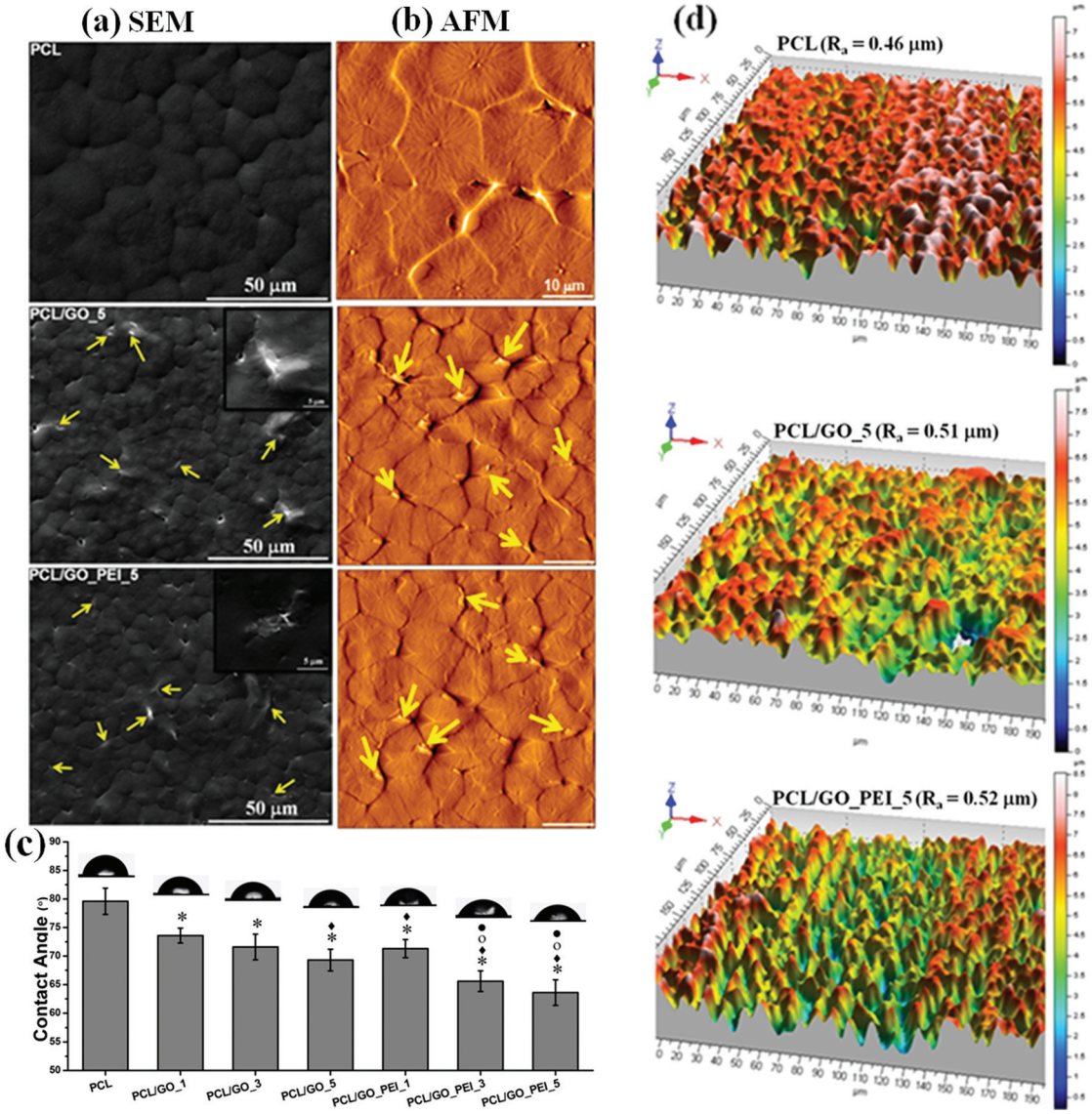


**Fig. 3** Surface characterization of PCL, PCL/GO_5 and PCL/GO_PEI films by (a) SEM, (b) AFM, (c) water contact angle goniometry on the different surfaces and (d) optical profilometry showing 3D surface profiles of neat PCL, PCL/GO_5 and PCL/GO_PEI_5. Statistically significant differences ($p < 0.05$) compared to PCL, PCL/GO_1, PCL/GO_3, and PCL/GO_PEI_1 are indicated by *, ◆, ○ and ●, respectively.

storage modulus of PCL increased with the loading fraction of graphene nanoparticles in PCL. The storage modulus of PCL increased from 374 MPa to 605 MPa and 492 MPa with the addition of 5 wt% GO and GO_PEI filler, respectively. The increase in the storage modulus of PCL composites may be attributed to stress transfer from the polymer matrix to well dispersed strong graphene nanoparticles. The PCL/GO composite showed higher enhancement in the storage modulus in comparison with PCL/GO_PEI composites. Note that the relatively lower modulus for PCL/GO_PEI may be attributed to the presence of a relatively low fraction of GO in GO_PEI. In this work, the filler content was fixed in the different composites (Table 1). In GO_PEI particles, the GO content is only ≈58 wt% of the particle, the rest being contributed by the polymer chains as determined by TGA such that the GO content in PCL/GO_PEI_5 is ≈2.9 wt% GO. The modulus of PCL/GO_PEI_5 is similar to that of PCL/GO_3, suggesting that GO_PEI is as effective as GO in enhancing the mechanical properties of PCL.

### 3.3 Cell proliferation

hMSCs in the bone marrow are the stem cells that differentiate to eventually form the bone tissue and thus have been used to evaluate the osteoconductivity of the composites. hMSC attachment and proliferation on PCL, PCL/GO and PCL/GO_PEI composites was assessed using a combination of DNA quantification (Fig. 4(a)) and fluorescence imaging (Fig. S3†) at day 1, 3 and 7. DNA content is taken as a measure of cell

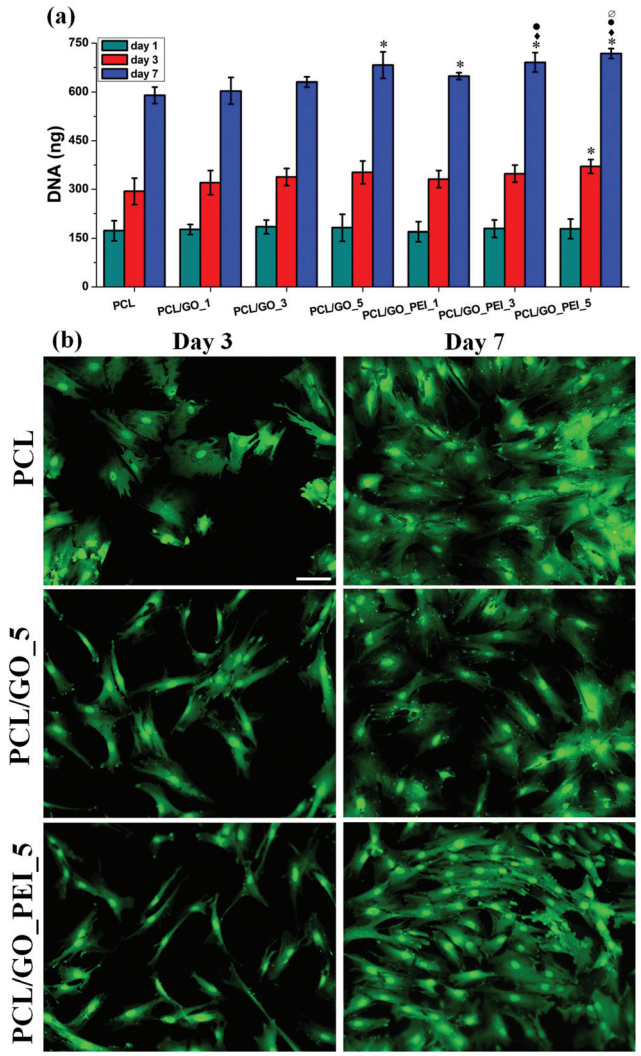


Fig. 4 (a) DNA quantification on PCL and its different composites at 1, 3 and 7 days after cell seeding. Statistically significant differences ($p < 0.05$) compared to PCL, PCL/GO_1, PCL/GO_3 and PCL/GO_PEI_1 are indicated by *, ◆, ○, and ∅ respectively. (b) Live/dead fluorescence micrographs of hMSCs on PCL, PCL/GO_5 and PCL/GO_PEI_5 (scale bar = 100 μm). Live cells are green and dead cells, if any, are red.

numbers. At day 1, neat PCL and both the composite films showed a similar DNA content suggesting no discernable difference in cell attachment. DNA content on all the spin coated samples increased from day 1 to day 3 and further by day 7, suggesting that hMSCs proliferated well on all surfaces. Interestingly, only the PCL/GO_PEI_5 composite showed significantly more DNA content than neat PCL. At day 7, PCL/GO_5 and all the PCL/GO_PEI composite films showed significantly higher DNA content in comparison with neat PCL. Most cells were observed on PCL/GO_PEI_5 with a 22% increase compared to neat PCL at day 7. Although both fillers augmented stem cell proliferation on PCL, these results indicate that the addition of GO_PEI was more effective than GO. Fluorescence micrograph images (Fig. S3†) show the increase in the number of cell nuclei on all the samples, confirming hMSC proliferation. Also, at day 7 more cells were seen on PCL/GO_PEI composite films especially on PCL/GO_PEI_5, corroborating the quantification from the DNA content assay. Representative micrographs of hMSCs on PCL, PCL/GO_5 and PCL/GO_PEI_5 substrates stained with live/dead dyes at day 3 and 7 are shown in Fig. 4(b). hMSCs were viable (green) on all the substrates and essentially no dead cells (red) were observed. Also, more cells could be seen at day 7 than at day 3. All these results suggested that hMSCs were metabolically active and proliferating on these substrates with no apparent toxicity from the reinforced graphene particles even at 5 wt%.

The initial interactions between cells and biomaterials are mediated by protein adsorption.[50] The surface charge and chemical properties of the biomaterial profoundly influence surface wettability, which in turn governs the nature of the adsorbed protein layer. Surfaces with different chemical functional groups provided a range of hydrophilicity with different surface charges.[51] Hydrophilic surfaces showed higher levels of protein adsorption which promoted cell adhesion and spreading. The enhanced proliferation on PCL/GO_PEI can be attributed to the hydrophilic and polycationic nature of the PEI decorated GO. Kim *et al.* reported that blending of cationic PEI in PCL improved surface wettability, resulting in an increase in cell attachment and proliferation.[22] Similarly, Qi *et al.* showed that a composite GO and cationic poly-L-lysine (PLL) prepared by the layer-by-layer technique provided a suitable environment for MSC attachment and growth.[27] Aside from the chemical moieties, the GO and GO_PEI particles at the surface of the composite (Fig. 3(a)) provide nanotopographic cues for cell attachment. Nanotopography plays an important role in controlling stem cell fate on biomaterial surfaces.[52] GO-coated glass were shown to provide nanoscale topographical cues for the attachment, proliferation and differentiation of human adipose-derived stem cells.[53] Hence, GO functionalized with PEI provided the synergetic effect of the chemical cues from the hydrophilic GO and polycationic PEI along with topographical cues for augmenting stem cell attachment and proliferation on PCL/GO_PEI.

### 3.4 Cell morphology

Early cell–biomaterial interactions influence cell morphology and spreading, which in turn is critical in determining cell proliferation and differentiation.[54] Stem cell morphology is reported to regulate stem cell fate.[55] Thus, we evaluated hMSC morphology on the different surfaces. Fig. 5(a) and (b) show the cell area and aspect ratio on the composites at day 1. The area of hMSCs decreased on the composites with an increase in the content of GO and GO_PEI. PCL/GO_5, PCL/GO_PEI_3 and PCL/GO_PEI_5 films induced 45%, 46% and 49% statistically significant reduction in the cell area compared to neat PCL. Furthermore, we evaluated the aspect ratio of cells on the neat PCL, PCL/GO_5 and PCL/GO_PEI_5 composites and compared them with neat PCL (Fig. 5(b)). hMSCs on neat PCL showed a greater number of large round cells whereas cells were more elongated on the composites. 93% of cells on PCL showed aspect ratios ≤2.5. The aspect ratio of hMSCs

 

increased on PCL/GO_5 and PCL/GO_PEI_5 composite films. 50% and 55% of cells on PCL/GO_5 and PCL/GO_PEI_5, respectively, showed aspect ratios between 4 and 7.5, whereas 21% and 27% of cells on PCL/GO_5 and PCL/GO_PEI_5 showed aspect ratios in the range of 7.5–12.5.

Fig. 5(c) shows representative fluorescence micrographs of hMSCs on neat PCL, PCL/GO_5 and PCL/GO_PEI_5 at day 1 and day 3. hMSCs on the composites showed a spindle-like elongated morphology with multi-branched filopodial protruded extensions, whereas most hMSCs were equiaxial on neat PCL. At day 3, a few cells on the PCL surface showed an elongated morphology although most of the hMSCs were round in shape. hMSCs on PCL/GO_5 and PCL/GO_PEI_5 maintained the elongated and branched morphologies. Spindle-shaped, elongated and branched morphologies of hMSCs observed on PCL/GO_5 and PCL/GO_PEI_5 composite films can be attributed to the presence of polar functionalized graphene (GO and GO_PEI). Several reports have shown that elongated stem cells with multi-branched morphology are an early indicator of osteogenesis.[56,57] Cells on hydrophilic surfaces showed an elongated morphology in contrast to rounded cells on hydrophobic surfaces.[58] Surfaces rich in amine and carboxyl groups preferentially orient the conformation of adsorbed proteins to promote the binding of integrins in osteoblasts to activate osteogenic differentiation pathways.[59] MSCs on glass coated with graphene particles exhibited an elongated spindle morphology leading to osteogenic lineage commitment.[60] Thus, the functionalized graphene nanoparticles in PCL were expected to promote hMSC osteogenesis as suggested by the early profound changes in cell morphology.

Fluorescence micrographs in Fig. 5(d) reveal that hMSCs on the composites showed more paxillin staining in comparison with neat PCL. hMSCs on neat PCL showed cell centered paxillin expression, whereas hMSCs on PCL/GO_5 and the PCL/GO_PEI_5 composite showed paxillin rich focal adhesions also at the tips of cellular protrusions (Fig. 5(d) as indicated by the arrows). The shift in paxillin position and higher paxillin expression suggests more and stronger focal adhesions on the composites. The ability of cells to sense different biomaterial surfaces involves integrin-mediated focal adhesion signaling. Studies have shown that focal adhesion meditates cell–material signaling eliciting downstream biochemical signals regulating stem cell fate.[61] Addition of GO and GO_PEI to PCL altered its surface chemistry and the nanotopographic features. As a result, hMSCs stained with an immunofluorescence antibody to paxillin (a focal adhesion protein) showed enhanced focal adhesions on PCL/GO_5 and PCL/GO_PEI_5 compared to neat PCL. Higher paxillin expression mediates cell spreading and mobility; as a result, cells with more focal adhesions have been shown to spread and elongate more. Furthermore, the increased focal adhesion accelerates proliferation and favors hMSC osteogenic differentiation.[61] Stem cells on nanotopographic and amine functionalized surfaces show better cell spreading and differentiation, which is attributed to integrin mediated focal adhesion signaling.[62,63]

### 3.5 Osteogenic differentiation

Fig. 6(a) presents ALP expression by hMSCs on PCL, PCL/GO_5 and PCL/GO_PEI_5. At day 14, hMSCs in osteogenic medium showed higher ALP expression than in growth medium. PCL/GO_5 and PCL/GO_PEI_5 showed ≈31 and ≈87% more ALP expression than PCL in osteogenic medium. At day 21, ALP expression declined in osteogenic medium, although PCL/GO_PEI_5 and PCL/GO_5 showed significantly higher ALP activity compared to neat PCL. In growth medium, hMSCs showed a slow and steady increase in ALP activity from day 14 to day 21. Note that even in growth medium, ALP activity was the highest on PCL/GO_PEI_5 followed by PCL/GO_5 and was the lowest for PCL. Taken together, PCL/GO_PEI_5 surfaces were most effective in inducing hMSCs to express ALP. ALP expression is the most common early marker used for osteogenic differentiation. Generally, ALP activity of stem cells peaks and then declines followed by mineral deposition. As a result, in osteogenic medium after 14 days, ALP expression decreased on all samples. However in growth medium, ALP expression was slow but increased steadily from day 14 to 21. This suggests, not surprisingly, that osteogenesis is enhanced and more rapid in osteogenic medium than in growth

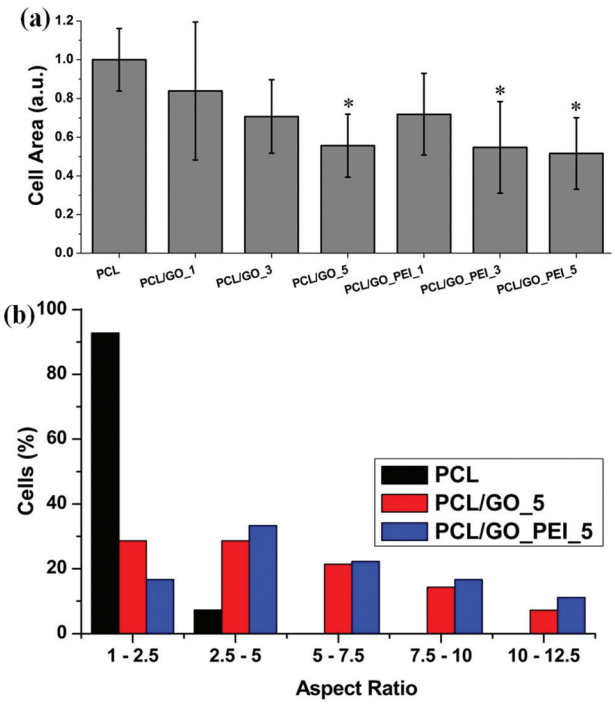


Fig. 5 (a) hMSC area analysis of PCL and its different composites after 1 day of cell seeding; (b) aspect ratio measurement of hMSCs on PCL, PCL/GO_5 and PCL/GO_PEI_5 films at day 1; (c) representative fluorescence micrographs showing cell morphology on PCL, PCL/GO_5 and PCL/GO_PEI_5 films at day 1 and day 3 (scale bar = 200 μm) and (d) focal adhesion Paxillin immunofluorescence micrograph of hMSCs on PCL, PCL/GO_5 and PCL/GO_PEI_5 surfaces (scale bar = 20 μm). Statistically significant differences ($p < 0.05$) compared to PCL, PCL/GO_1, PCL/GO_3, and PCL/GO_PEI_1 are indicated by *, ◆, ● and ∅, respectively.

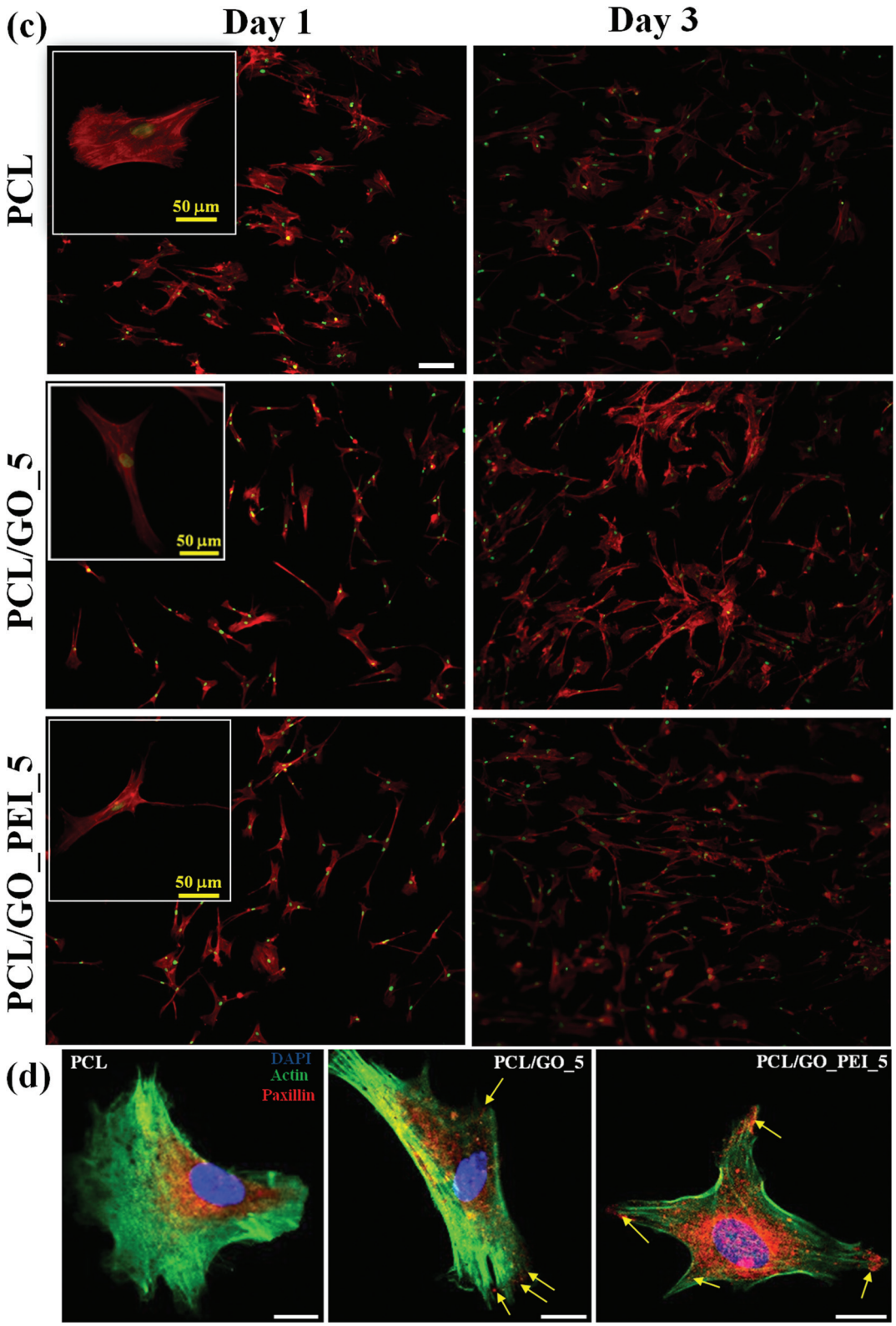


Fig. 5 *(Contd)*.

medium. Studies have shown that graphene particles help in osteogenic induction resulting in high ALP expression by cells.[8] Thus, the addition of GO and GO_PEI led to increased ALP expression by hMSCs on the composite films in comparison with neat PCL. Amine functionalized surface and GO functionalized with positively charged poly-L-lactic acid (GO–PLL)

 

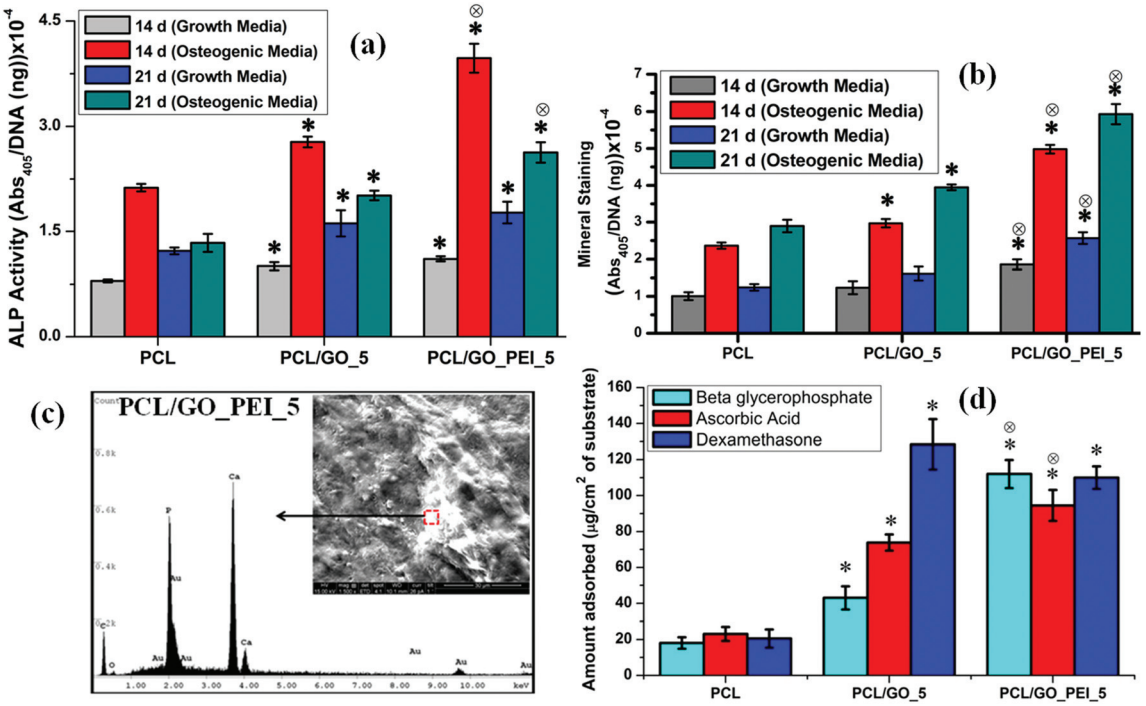


**Fig. 6** Evaluation of osteogenic differentiation of hMSCs: (a) ALP activity of hMSCs on PCL, PCL/GO_5 and PCL/GO_PEI_5 films in growth and osteogenic supplement media at day 14 and 21; (b) mineral quantification at day 14 and 21 using ARS dye, (c) EDAX spectra with the inset showing SEM micrographs of mineral deposited PCL/GO_PEI_5 and (d) adsorption of osteogenic factors on PCL, PCL/GO_5 and PCL/GO_PEI_5. Statistically significant differences ($p < 0.05$) compared to PCL, PCL/GO_1, PCL/GO_3, PCL/GO_5, PCL/GO_PEI_1 and PCL/GO_PEI_3 are indicated by *, ◆, ●, ⊗, ∅ and Φ respectively.

enhance osteogenic gene expression and ALP activity owing to enhanced integrin mediated focal adhesion and adsorption of osteogenic factors.[27,62]

Differences in surface chemistry can influence differentiation of multipotential stem cells into different lineages.[62,64] We studied the mineralization resulting from osteogenic differentiation of hMSCs on the neat polymer and the composites. Fig. S4(a)† shows the mineral content determined by ARS on PCL and its different composites (in the presence of osteogenic supplements). At both day 14 and 21, mineral content scaled with the filler content. At day 14, PCL and PCL/GO_1 showed similar mineral contents, whereas other composites showed significantly higher mineral content. The largest mineral content was observed in PCL/GO_PEI_5 followed by PCL/GO_PEI_3 and PCL/GO_5. At day 21, mineral deposited by cells increased on all the surfaces. PCL/GO_PEI_5 showed ≈90% more mineral content compared to neat PCL, whereas PCL/GO_PEI_3 and PCL/GO_5 showed ≈44% and ≈36% more mineral content, respectively. Since 5 wt% graphene content in the PCL matrix (PCL/GO_5 and PCL/GO_PEI_5) showed the highest mineralization, we further studied the ability of GO and GO_PEI composites to induce osteogenesis in growth medium in the absence of soluble factors. Fig. 6(b) shows a quantitative comparison of mineral deposition by hMSCs on PCL, PCL/GO_5 and PCL/GO_PEI_5 composites at day 14 and 21. As expected, the mineral deposition in the absence of the osteogenic supplements was lower than that in their presence. Interestingly, PCL/GO_PEI showed ≈70% and ≈95% higher mineral deposition than neat PCL in growth medium at day 14 and 21. Remarkably, PCL/GO_PEI_5 in growth medium at day 14 yielded ≈79% on neat PCL in the presence of osteogenic factors and at day 21 nearly the same amount of mineral (≈90%, no statistical difference) demonstrating that GO_PEI is exceptionally potent in inducing stem cell osteogenesis.

Fig. S4(b)† shows the digital image of ARS (red) stained minerals deposited by hMSCs on neat PCL, PCL/GO_5 and PCL/GO_PEI_5 at day 21. These images qualitatively corroborate the quantification in Fig. 6(b). SEM micrographs of hMSCs on these different surfaces showed bright mineral deposits in the form of nodules and EDAX revealed the chemical composition. Fig. 6(c) shows a representative SEM micrograph and the EDAX spectra of the mineralized surface of PCL/GO_PEI_5. The EDAX spectrum shows the presence of calcium and phosphate confirming the characteristic composition of the mineral deposits.

It has been reported that hMSCs cultured on a bioactive surface in the presence of osteogenic supplements results in the induction of osteogenic differentiation and mineral deposition.[65] ALP activity and mineralization results revealed that PCL/GO and PCL/GO_PEI composites showed better osteogenic differentiation than neat PCL although GO_PEI was markedly more efficient. It has been demonstrated that GO nanoparticles have a strong affinity to adsorb osteogenic supplements such as dexamethasone and β-glycerophosphate on

its surface, which in turn promotes osteogenic differentiation of stem cells.[4] In addition, Qi *et al.* have reported that GO/PLL (poly-L-lactic acid) showed a high adsorption of osteogenic supplements due to π–π interactions between graphene and dexamethasone, and electrostatic interactions between anionic β-glycerol phosphate and cationic PLL. High adsorption of osteogenic factors to the GO/PLL film promoted osteogenic differentiation of MSCs.[27] Studies have shown that polymer surfaces having functional groups such as carboxyl and amine were effective in binding calcium and phosphate ions.[66,67] Reinforcement of amine-functionalized carbon nanotubes in PCL was shown to promote osteogenic differentiation and mineralization.[68] GO functionalized with amine groups presenting both carboxyl and amine functional groups were also effective in promoting mineralization as shown in our previous study for PCL composites containing MDA-functionalized GO.[19] Enhanced mineralization on PCL/GO_PEI composites can be attributed to the synergetic effect of the chemical functional groups on the functionalized GO, which likely regulated the adsorption of osteogenic factors and facilitated nucleation of hydroxyapatite. Whereas the mineral content on the PCL composite containing 5% MDA-modified GO was 40% higher than that on neat PCL,[19] here we observe a near doubling demonstrating the potent ability of GO_PEI to induce osteogenic differentiation of hMSCs. In this study, PEI/PAA functionalized GO provides a significantly higher density of amine and carboxyl groups resulting in the large increase of stem cell osteogenesis compared to neat PCL.

Keselowsky *et al.* observed that biomaterial surfaces with –OH and $–NH_2$ chemical moieties showed up-regulation of osteogenic gene expression leading to enhanced mineralization.[59] Amine-modified surfaces were shown to promote focal adhesions enhancing differentiation and mineralization.[69] In another study, $–NH_2$ modified surface promoted the osteogenesis of stem cells both in the presence and absence of osteogenic factors.[70] Thus, GO_PEI rich in amine groups and oxygen containing functional groups are as effective as osteoinductive factors. Conventionally, for bone tissue regeneration applications, biomolecules such as bone morphogenic proteins (BMP) and other osteogenic factors have been widely used to modify biomaterials.[71] Biomolecules such as growth factors are expensive and labile, thereby limiting the routes available for processing of the biomaterial. In contrast, GO_PEI can yield bioactive materials without limitations of stability and choice of processing routes associated with biomolecules.

### 3.6 Adsorption of osteogenic factors

We further investigated the role of the nanofillers in the adsorption of osteogenic factors present in the culture medium in driving osteogenic differentiation of stem cells. Studies have demonstrated that a surface with high affinity for osteogenic factors directly influences osteogenic differentiation of stem cells.[4,27] Graphene and its derivatives have a remarkable ability to adsorb biomolecules such as proteins and DNA due to the high surface area and weak interactions.[72,73]

Fig. 6(d) shows the adsorption of β-glycerol phosphate, dexamethasone and ascorbic acid on neat PCL and PCL/GO_5 and PCL/GO_PEI_5 surfaces. PCL/GO_5 and PCL/GO_PEI_5 composites adsorbed more of each of the three factors than neat PCL. A markedly higher amount (112 μg $cm^{-2}$) of β-glycerol phosphate was adsorbed on the PCL/GO_PEI_5 surface compared to 43 μg $cm^{-2}$ and 18 μg $cm^{-2}$ for PCL/GO_5 and PCL, respectively. The presence of cationic PEI molecules on the GO_PEI surface likely results in electrostatic attraction for the adsorption of anionic phosphates to enhance adsorption.[27] Adsorption of dexamethasone to PCL/GO and PCL/GO_PEI composites was similar but higher than that on neat PCL. Adsorption of dexamethasone on GO and GO_PEI exposed at the surface may be attributed to weak π–π interactions between the aromatic rings of dexamethasone and the basal planes of graphene.[4] In the case of ascorbic acid, the highest adsorption was seen on PCL/GO_PEI followed by PCL/GO and neat PCL. Studies have demonstrated that adsorption of ascorbic acid is mediated by hydrogen bonding with the substrate.[4,74] We thus evaluated the adsorbed ascorbic acid on the composite surface by the attenuated total reflection FTIR method (ATR-FTIR). Fig. S5† presents the FTIR spectra of the adsorbed ascorbic acid. As discussed in more detail in the ESI,† the increased adsorption of ascorbic acid to PCL/GO_PEI_5 may be ascribed to the intermolecular coupling mediated by hydrogen bonding between ascorbic acid and GO_PEI. The increased presence of polar groups on GO_PEI than on GO facilitates greater hydrogen bonding with ascorbic acid. These adsorption results demonstrate that PCL/GO_PEI is most efficient in adsorption of the osteogenic factors followed by PCL/GO and lastly neat PCL. Thus, the differential adsorption behavior plays a critical role in the enhanced osteogenesis of stem cells on PCL/GO_PEI composites.

### 3.6 Antibacterial activity

In biomedical applications, complications arising from bacterial infections are a major source of implant rejection, and repeat surgical procedures thereby constitute a significant clinical challenge. Thus, fillers that induce minimal toxicity to mammalian cells and yet minimize bacterial infection by either resisting attachment or imparting bactericidal activity are highly attractive. Antibacterial properties of biomaterials are governed by the surface physical and chemical properties.[75] Studies have shown that chemically modified biomaterial surfaces prevent bacterial attachment and biofilm formation.[75] Similarly, Pasquini *et al.* demonstrated the effect of different chemically functionalized carbon nanotubes on bacterial cytotoxicity.[76]

Fig. 7(a) and (b) show the relative CFU counts and viable bacterial colonies grown on agar plates for PCL, PCL/GO and PCL/GO_PEI in a direct contact test. PCL/GO and PCL/GO_PEI composites showed strong antibacterial activity on its surface. Bacterial colonies decreased with increasing graphene content suggesting that the antibacterial properties of the composites

 

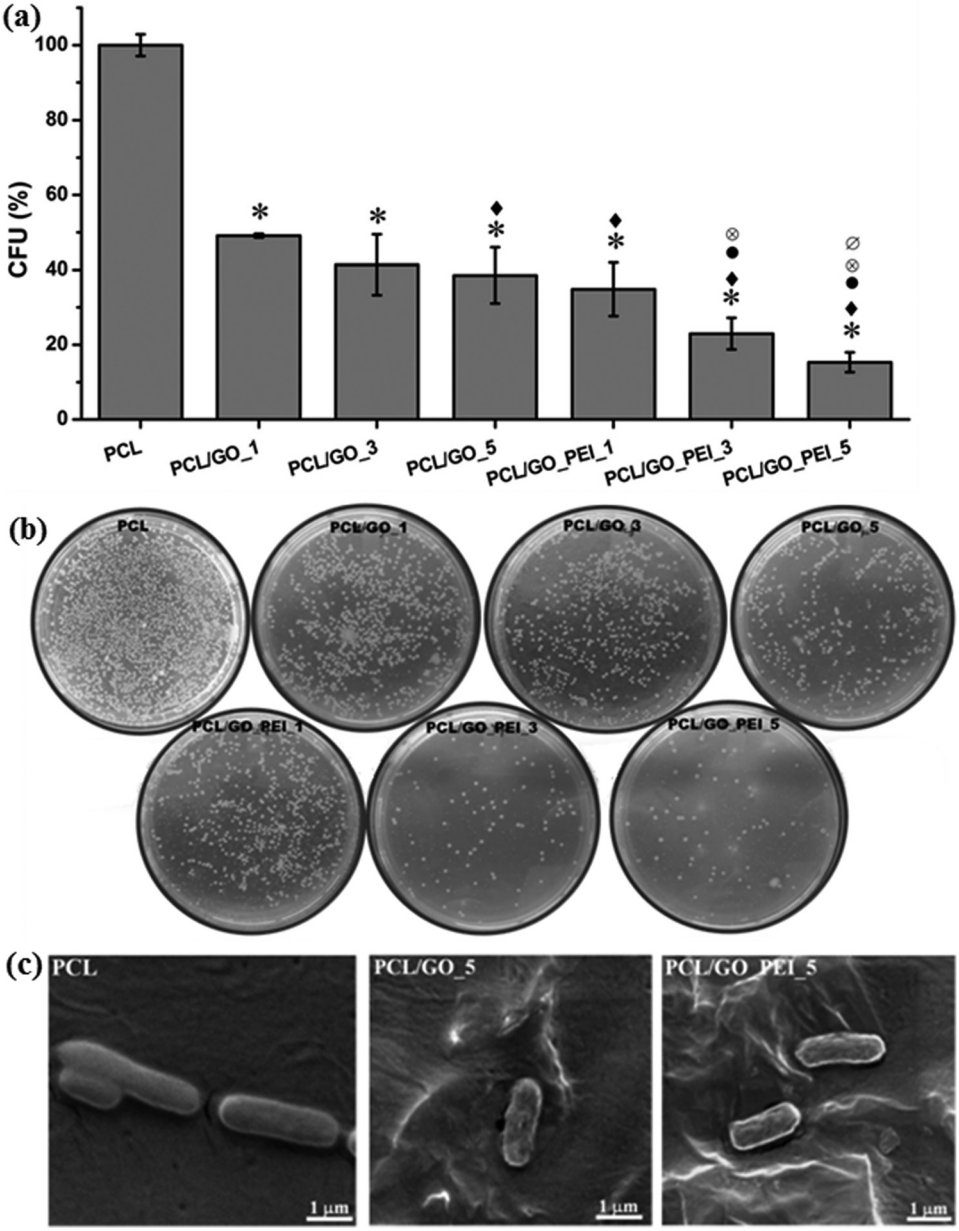


Fig. 7 Antibacterial study showing (a) colony count of *E. coli* on the different composites with respect to neat PCL. (b) Photographs of viable *E. coli* colonies grown on LB agar plates. (c) SEM micrographs of bacterial morphology on PCL, PCL/GO_5 and PCL/GO_PEI_5 surfaces.

scaled with the filler content. The PCL/GO_PEI_5 composite showed the largest decrease in bacterial colonies with only 15% of that of neat PCL whereas PCL/GO_5 showed a corresponding value of 38%.

Viability of the *E. coli* adhered to these surfaces was independently assessed by live/dead staining. Fig. S6† shows fluorescent micrographs of live cells (stained green) and dead cells (stained red) on PCL, PCL/GO and PCL/GO_PEI surfaces. Most of the cells on the PCL surface were viable. Addition of GO and GO_PEI into PCL showed a bactericidal effect confirmed by the appearance of more dead cells on the PCL/GO and PCL/GO_PEI surfaces. With the increase in the GO and GO_PEI content the fraction of nonviable bacterial cells increased. Live/dead staining of bacterial cells on the different samples corroborates the results from the colony count assay. These results suggest that the addition of GO and GO_PEI particles imparts antibacterial activity to PCL.

SEM micrographs reveal the nature of cell–material interactions underlying the antibacterial activity of PCL/GO and PCL/GO_PEI composites. The PCL film was covered by a large number of bacterial cells that were arranged into colonies, an early stage of biofilm formation. In contrast, PCL/GO and PCL/GO_PEI composites showed fewer bacteria that were adhered as individual cells, suggesting resistance to biofilm formation (Fig. S7†). Furthermore, SEM micrographs reveal damage to the bacterial membrane integrity induced by GO and GO_PEI

exposed at the surface (Fig. 7(c)). Bacterial cells exhibited a rough and flattened morphology and the membrane appeared severely disrupted on PCL/GO and PCL/GO_PEI surfaces in contrast to the smooth cells on PCL. The bacterial membrane damage upon contact with GO was presumably caused by the sharp edges of the graphene particles that induce a loss of membrane integrity and result in glutathione oxidation.[77] Also, GO sheets can increase cellular oxidative stress in bacteria without producing superoxide anions.[13]

The antibacterial activity of PCL/GO_PEI may be attributed to the synergetic effect of GO and the conjugated PEI polymer. Polycationic polymers like PEI have shown contact-active bactericidal activity by disrupting the Gram negative bacterial membrane leading to cell lysis.[78] The cationic nature of PEI resulting from the multiple amine groups causes electrostatic interactions with the negatively charged phospholipid molecules on the bacterial membrane. Such interactions can result in the inversion and lateral movement of the negatively charged lipids generated in holes in the lipid bilayer of the bacterial membrane, causing leakage of the cytoplasm and eventually cell death.[79,80] The cytoplasm of leaking bacterial cells will appear thinner and flatter morphologically as seen in the SEM micrographs (Fig. 7(c)).

The GO_PEI composites showed remarkably better antibacterial properties compared to our previous results with GO–MDA composites.[19] Whereas 5% GO–MDA in PCL reduced the colony counts to 40% of neat PCL, GO_PEI was more than twice as effective with a reduction in the colony count to 15%. The exceptional antibacterial property of GO_PEI can be attributed to the presence of more free amine groups on GO in contrast to MDA functionalized GO, which provides more active cationic groups for bactericidal activity. Furthermore, the use of PAA as the linker molecule to conjugate PEI to GO likely provides additional mobility to the positively charged polymer brush to interact with bacteria.

## 4. Conclusion

GO_PEI sheets were synthesized using PAA as a spacer on GO and characterized using a variety of techniques. PCL composites of GO and GO_PEI were prepared by the spin coating technique with varying filler contents. Addition of GO and GO_PEI increased surface wettability, surface roughness and modulus of PCL. *In vitro* cell studies revealed that GO_PEI composites promoted proliferation and focal adhesions in hMSCs. GO_PEI was highly potent in inducing stem cell osteogenesis and mineralization, and was markedly better than GO. This response was attributed to the multiple free amine and oxygen containing functional groups on GO_PEI along with increased nanoscale roughness of the surface. PEI_GO having amine and oxygen containing polar functional groups further promotes adsorption of osteogenic factors for enhanced differentiation. Bacterial studies revealed that the addition of GO and GO_PEI induced bacterial membrane damage upon contact leading to death. GO_PEI exhibited an exceptionally high antibacterial property, which may be attributed to the synergetic effect of the sharp edges of the nanoparticles and the chemical moieties of the grafted polymeric chains. Taken together, through enhanced cell proliferation, remarkable osteoinductive potential and exceptional bactericidal activity, GO_PEI is shown to impart multi-biofunctional properties to PCL. Thus, GO_PEI-based polymer composites can find potential use in orthopedics to fabricate bioresorbable fracture fixation devices and tissue scaffolds as an alternative to the use of labile biomolecules in preparing bioactive materials.

## Acknowledgements

This work was funded by the Department of Science and Technology (DST), India. K. C. acknowledges a Ramanujan fellowship from DST. The authors gratefully acknowledge support from Mr Shyam Sundar for contact angle measurements and Mr Prasanna Kumar S. Mural for Raman spectroscopy. Access to equipment at the Advanced Facility for Microscopy and Microanalysis (AFMM) in IISc is acknowledged.

## References

1 Y. Liu, D. Yu, C. Zeng, Z. Miao and L. Dai, *Langmuir*, 2010, **26**, 6158–6160.
2 L. Zhang, Y. Xing, N. He, Y. Zhang, Z. Lu, J. Zhang and Z. Zhang, *J. Nanosci. Nanotechnol.*, 2012, **12**, 2924–2928.
3 L. Zhang, J. Xia, Q. Zhao, L. Liu and Z. Zhang, *Small*, 2010, **6**, 537–544.
4 W. C. Lee, C. H. Y. Lim, H. Shi, L. A. Tang, Y. Wang, C. T. Lim and K. P. Loh, *ACS Nano*, 2011, **5**, 7334–7341.
5 K. Sarkar, G. Madras and K. Chatterjee, *RSC Adv.*, 2015, **5**, 50196–50211.
6 I. E. M. Carpio, C. M. Santos, X. Wei and D. F. Rodrigues, *Nanoscale*, 2012, **4**, 4746–4756.
7 E. Kolanthai, S. Bose, K. Bhagyashree, S. Bhat, K. Asokan, D. Kanjilal and K. Chatterjee, *Phys. Chem. Chem. Phys.*, 2015, **17**, 22900–22910.
8 N. Dubey, R. Bentini, I. Islam, T. Cao, A. H. C. Neto and V. Rosa, *Stem Cells Int.*, 2015, 2015.
9 K. Rezwan, Q. Chen, J. Blaker and A. R. Boccaccini, *Biomaterials*, 2006, **27**, 3413–3431.
10 T. R. Nayak, H. Andersen, V. S. Makam, C. Khaw, S. Bae, X. Xu, P.-L. R. Ee, J.-H. Ahn, B. H. Hong and G. Pastorin, *ACS Nano*, 2011, **5**, 4670–4678.
11 Y. C. Shin, J. H. Lee, O. S. Jin, S. H. Kang, S. W. Hong, B. Kim, J.-C. Park and D.-W. Han, *Carbon*, 2015, **95**, 1051–1060.
12 T. K. Das and S. Prusty, *Polym.-Plast. Technol. Eng.*, 2013, **52**, 319–331.
13 S. Liu, T. H. Zeng, M. Hofmann, E. Burcombe, J. Wei, R. Jiang, J. Kong and Y. Chen, *ACS Nano*, 2011, **5**, 6971–6980.
14 J. Park, P. Kim, W. Helen, A. J. Engler, A. Levchenko and D.-H. Kim, *Integr. Biol.*, 2012, **4**, 1008–1018.

 

15 S. Ding and P. G. Schultz, *Nat. Biotechnol.*, 2004, **22**, 833–840.
16 T.-H. Kim, S. Shah, L. Yang, P. T. Yin, M. K. Hossain, B. Conley, J.-W. Choi and K.-B. Lee, *ACS Nano*, 2015, **9**, 3780–3790.
17 Y. C. Shin, J. H. Lee, O. S. Jin, S. H. Kang, S. W. Hong, B. Kim, J.-C. Park and D.-W. Han, *Carbon*, 2015, **95**, 1051–1060.
18 S. Kumar and K. Chatterjee, *Nanoscale*, 2015, **7**, 2023–2033.
19 S. Kumar, S. Raj, E. Kolanthai, A. K. Sood, S. Sampath and K. Chatterjee, *ACS Appl. Mater. Interfaces*, 2015, **7**, 3237–3252.
20 W. Godbey, K. K. Wu and A. G. Mikos, *J. Controlled Release*, 1999, **60**, 149–160.
21 A. R. Vancha, S. Govindaraju, K. V. Parsa, M. Jasti, M. González-García and R. P. Ballestero, *BMC Biotechnol.*, 2004, **4**, 23.
22 J. H. Kim, P.-H. Choung, I. Y. Kim, K. T. Lim, H. M. Son, Y.-H. Choung, C.-S. Cho and J. H. Chung, *Mater. Sci. Eng., C*, 2009, **29**, 1725–1731.
23 B. Chen, M. Liu, L. Zhang, J. Huang, J. Yao and Z. Zhang, *J. Mater. Chem.*, 2011, **21**, 7736–7741.
24 Y. Weng, B. Jiang, K. Yang, Z. Sui, L. Zhang and Y. Zhang, *Nanoscale*, 2015, **7**, 14284–14291.
25 W. S. Hummers Jr. and R. E. Offeman, *J. Am. Chem. Soc.*, 1958, **80**, 1339–1339.
26 S. Kumar, M. Azam, S. Raj, E. Kolanthai, K. Vasu, A. Sood and K. Chatterjee, *J. Biomed. Mater. Res., Part B*, 2015, DOI: 10.1002/jbm.b.33549.
27 W. Qi, W. Yuan, J. Yan and H. Wang, *J. Mater. Chem. B*, 2014, **2**, 5461–5467.
28 E. Weiss, M. Shalhav and Z. Fuss, *Dent. Traumatol.*, 1996, **12**, 179–184.
29 F. o. Perreault, M. E. Tousley and M. Elimelech, *Environ. Sci. Technol. Lett.*, 2013, **1**, 71–76.
30 T. Kavitha, I.-K. Kang and S.-Y. Park, *Langmuir*, 2013, **30**, 402–409.
31 Y. Chen, Y. Qi and B. Liu, *J. Nanomater.*, 2013, **2013**, 16.
32 Z. Tai, H. Ma, B. Liu, X. Yan and Q. Xue, *Colloids Surf., B*, 2012, **89**, 147–151.
33 P.-G. Ren, D.-X. Yan, X. Ji, T. Chen and Z.-M. Li, *Nanotechnology*, 2011, **22**, 055705.
34 F. Wang, P. Liu, T. Nie, H. Wei and Z. Cui, *Int. J. Mol. Sci.*, 2012, **14**, 17–29.
35 H. Kim, R. Namgung, K. Singha, I.-K. Oh and W. J. Kim, *Bioconjugate Chem.*, 2011, **22**, 2558–2567.
36 T. Tsoufis, F. Katsaros, Z. Sideratou, B. J. Kooi, M. Karakassides and A. Siozios, *Chem. – Eur. J.*, 2014, **20**, 8129–8137.
37 L. Cao, Q. Sun, Y. Gao, L. Liu and H. Shi, *Electrochim. Acta*, 2015, **158**, 24–34.
38 Y. Zhang, H.-L. Ma, Q. Zhang, J. Peng, J. Li, M. Zhai and Z.-Z. Yu, *J. Mater. Chem.*, 2012, **22**, 13064–13069.
39 H. Liu, T. Kuila, N. H. Kim, B.-C. Ku and J. H. Lee, *J. Mater. Chem. A*, 2013, **1**, 3739–3746.
40 J. Li, W. Tang, J. Huang, J. Jin and J. Ma, *Catal. Sci. Technol.*, 2013, **3**, 3155–3162.
41 L. Q. Xu, W. J. Yang, K.-G. Neoh, E.-T. Kang and G. D. Fu, *Macromolecules*, 2010, **43**, 8336–8339.
42 B. G. Choi, H. Park, T. J. Park, M. H. Yang, J. S. Kim, S.-Y. Jang, N. S. Heo, S. Y. Lee, J. Kong and W. H. Hong, *ACS Nano*, 2010, **4**, 2910–2918.
43 M. Fang, Z. Chen, S. Wang and H. Lu, *Nanotechnology*, 2012, **23**, 085704.
44 D. Graf, F. Molitor, K. Ensslin, C. Stampfer, A. Jungen, C. Hierold and L. Wirtz, *Nano Lett.*, 2007, **7**, 238–242.
45 L. Yang, B. Tang and P. Wu, *J. Mater. Chem. A*, 2014, **2**, 18562–18573.
46 G. Eda and M. Chhowalla, *Nano Lett.*, 2009, **9**, 814–818.
47 L. Hua, W. Kai, J. Yang and Y. Inoue, *Polym. Degrad. Stab.*, 2010, **95**, 2619–2627.
48 S. Wang, Y. Zhang, N. Abidi and L. Cabrales, *Langmuir*, 2009, **25**, 11078–11081.
49 J. Kim, Y.-R. Kim, Y. Kim, K. T. Lim, H. Seonwoo, S. Park, S.-P. Cho, B. H. Hong, P.-H. Choung and T. D. Chung, *J. Mater. Chem. B*, 2013, **1**, 933–938.
50 T. Akasaka, A. Yokoyama, M. Matsuoka, T. Hashimoto and F. Watari, *Mater. Sci. Eng., C*, 2010, **30**, 391–399.
51 K. Webb, V. Hlady and P. A. Tresco, *J. Biomed. Mater. Res.*, 1998, **41**, 422.
52 K.-C. Wu, C.-L. Tseng, C.-C. Wu, F.-C. Kao, Y.-K. Tu, E. C. So and Y.-K. Wang, *Sci. Technol. Adv. Mater.*, 2013, **14**, 054401.
53 J. Kim, K. S. Choi, Y. Kim, K. T. Lim, H. Seonwoo, Y. Park, D. H. Kim, P. H. Choung, C. S. Cho and S. Y. Kim, *J. Biomed. Mater. Res., Part A*, 2013, **101**, 3520–3530.
54 K. Anselme, *Biomaterials*, 2000, **21**, 667–681.
55 J. Folkman and A. Moscona, *Nature*, 1978, **273**, 345–349.
56 G. Kumar, C. K. Tison, K. Chatterjee, P. S. Pine, J. H. McDaniel, M. L. Salit, M. F. Young and C. G. Simon, *Biomaterials*, 2011, **32**, 9188–9196.
57 J. Kim, H. N. Kim, K.-T. Lim, Y. Kim, H. Seonwoo, S. H. Park, H. J. Lim, D.-H. Kim, K.-Y. Suh and P.-H. Choung, *Sci. Rep.*, 2013, 3.
58 J. Malmström, B. Christensen, J. Lovmand, E. S. Sørensen, M. Duch and D. S. Sutherland, *J. Biomed. Mater. Res., Part A*, 2010, **95**, 518–530.
59 B. G. Keselowsky, D. M. Collard and A. J. García, *Proc. Natl. Acad. Sci. U. S. A.*, 2005, **102**, 5953–5957.
60 M. Kalbacova, A. Broz, J. Kong and M. Kalbac, *Carbon*, 2010, **48**, 4323–4329.
61 W. Chen, L. G. Villa-Diaz, Y. Sun, S. Weng, J. K. Kim, R. H. Lam, L. Han, R. Fan, P. H. Krebsbach and J. Fu, *ACS Nano*, 2012, **6**, 4094–4103.
62 J. E. Phillips, T. A. Petrie, F. P. Creighton and A. J. García, *Acta Biomater.*, 2010, **6**, 12–20.
63 Y. Yang, K. Kulangara, R. T. Lam, R. Dharmawan and K. W. Leong, *ACS Nano*, 2012, **6**, 8591–8598.
64 D. S. Benoit, M. P. Schwartz, A. R. Durney and K. S. Anseth, *Nat. Mater.*, 2008, **7**, 816–823.
65 A. K. Gaharwar, S. M. Mihaila, A. Swami, A. Patel, S. Sant, R. L. Reis, A. P. Marques, M. E. Gomes and A. Khademhosseini, *Adv. Mater.*, 2013, **25**, 3329–3336.
66 J. Li, Y. Chen, Y. Yin, F. Yao and K. Yao, *Biomaterials*, 2007, **28**, 781–790.

67 W. J. Landis and R. Jacquet, *Calcif. Tissue Int.*, 2013, **93**, 329–337.
68 S. Kumar, S. Bose and K. Chatterjee, *RSC Adv.*, 2014, **4**, 19086–19098.
69 B. G. Keselowsky, D. M. Collard and A. J. García, *Biomaterials*, 2004, **25**, 5947–5954.
70 J. M. Curran, R. Chen and J. A. Hunt, *Biomaterials*, 2006, **27**, 4783–4793.
71 F. R. Rose and R. O. Oreffo, *Biochem. Biophys. Res. Commun.*, 2002, **292**, 1–7.
72 T. Alava, J. A. Mann, C. c. Théodore, J. J. Benitez, W. R. Dichtel, J. M. Parpia and H. G. Craighead, *Anal. Chem.*, 2013, **85**, 2754–2759.
73 J. S. Park, N.-I. Goo and D.-E. Kim, *Langmuir*, 2014, **30**, 12587–12595.
74 O. Akhavan, E. Ghaderi and M. Shahsavar, *Carbon*, 2013, **59**, 200–211.
75 K. Bazaka, M. V. Jacob, R. J. Crawford and E. P. Ivanova, *Appl. Microbiol. Biotechnol.*, 2012, **95**, 299–311.
76 L. M. Pasquini, S. M. Hashmi, T. J. Sommer, M. Elimelech and J. B. Zimmerman, *Environ. Sci. Technol.*, 2012, **46**, 6297–6305.
77 J. Chen, X. Wang and H. Han, *J. Nanopart. Res.*, 2013, **15**, 1–14.
78 L. Timofeeva and N. Kleshcheva, *Appl. Microbiol. Biotechnol.*, 2011, **89**, 475–492.
79 T. Ikeda, H. Yamaguchi and S. Tazuke, *Biochim. Biophys. Acta, Biomembr.*, 1990, **1026**, 105–112.
80 Y. He, E. Heine, N. Keusgen, H. Keul and M. Möller, *Biomacromolecules*, 2012, **13**, 612–623.